

Measurement of the π^- form factor

E. B. Dally,* D. J. Drickey,[†] J. M. Hauptman, C. F. May,[‡] and D. H. Stork
Physics Department, University of California at Los Angeles, Los Angeles, California 90024

J. A. Poirier, C. A. Rey,[§] and R. J. Wojslaw^{||}
Physics Department, University of Notre Dame, Notre Dame, Indiana 46556

P. F. Shepard
Department of Physics and Astronomy, University of Pittsburgh, Pittsburgh, Pennsylvania 15260

A. J. Lennox,[¶] J. C. Tompkins,** T. E. Toohig, and A. A. Wehmann
Fermi National Accelerator Laboratory, Batavia, Illinois 60510

I. X. Ioan,^{††} T. S. Nigmanov, E. N. Tsyganov, and A. S. Vodopianov
Joint Institute for Nuclear Research, Dubna, U.S.S.R.
 (Received 10 January 1980)

An experiment to measure the electromagnetic form factor of the negative π meson has been carried out at Fermilab by elastically scattering 100-GeV/c pions from the atomic electrons in a liquid-hydrogen target. We find that the elastic differential scattering cross section is characterized by a root-mean-square pion charge radius of 0.56 ± 0.04 fm. This paper describes our experimental design, measurement resolutions, event triggering logic, event reconstruction, experimental corrections, and form-factor results.

I. INTRODUCTION

The pion's electromagnetic form factor $F_\pi(q^2)$ can be defined by the relation

$$(d\sigma/dq^2)_{\text{exp}} = (d\sigma/dq^2)_{\text{pt}} |F_\pi(q^2)|^2, \quad (1.1)$$

where $(d\sigma/dq^2)_{\text{exp}}$ is the measured differential cross section for πe elastic scattering, $(d\sigma/dq^2)_{\text{pt}}$ is the predicted cross section for scattering of point pions by electrons, and q^2 is the square of the momentum transferred to the electron. This form factor can be related to the pion radius by expanding in a power series about $q=0$:

$$|F_\pi(q^2)| = 1 - \frac{1}{6} \langle r_\pi^2 \rangle q^2 + \dots, \quad (1.2)$$

where the coefficient of the first q^2 term is related to the mean-square radius of the pion's electromagnetic charge distribution by the expression

$$\langle r_\pi^2 \rangle = -6 [d|F_\pi(q^2)|/dq^2]_{q^2=0}. \quad (1.3)$$

We have measured the square of the form factor directly by scattering 100-GeV/c pions from atomic electrons in a liquid-hydrogen target and observing the departure of the measured differential cross section for elastic πe scattering from that of a point pion. The upper kinematic limit for πe scattering of 100-GeV/c incident pions is $q^2 = 0.084$ (GeV/c)². Thus, the experiment was sensitive to terms to order q^2 in Eq. (1.2), and our measurements may be characterized by a single parameter, the mean square charge radius $\langle r_\pi^2 \rangle$.

Our values for $\langle r_\pi^2 \rangle$ and $F_\pi(q^2)$ have already been reported.¹ In this paper we give details of the experimental setup and the method of data reduction (including important corrections to the cross section), and discuss our results in comparison with both the predicted values from some form-factor models and the measured values obtained using other experimental approaches.

II. EXPERIMENTAL SETUP AND PROCEDURE

A. Introduction

The three major factors influencing the design of the experiment were the kinematic characteristics of elastic πe scattering, the relative magni-

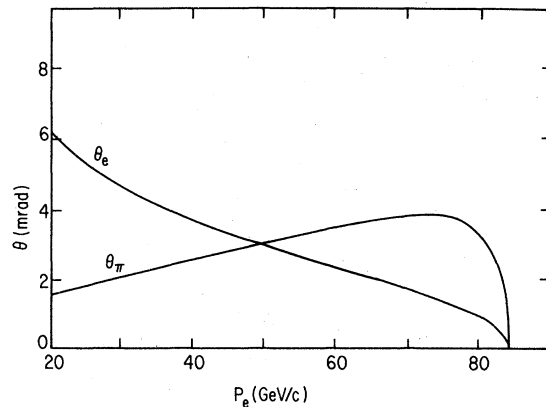


FIG. 1. πe elastic angular kinematics as a function of recoil-electron momentum at 100-GeV/c incident-pion momentum.

tudes of the cross sections for background interactions, and the practical experience gained in a similar experiment performed previously at Serpukhov.² Kinematic considerations can be understood by studying Fig. 1, which shows the pion and electron scattering angles as a function of the momentum of the scattered electron in the laboratory frame. It is clear that the small angles between the scattered particles required a detector with good spatial and angular resolution, while the small range of scattering angles allowed for the design of a magnetic spectrometer with nearly 100% geometric efficiency. The second factor influencing the experimental design was the need to eliminate background due to strong interactions having cross sections three or four orders of magnitude greater than the πe cross section. To exploit fully the energy and momentum constraints of elastic scattering, the experiment was designed to measure all kinematic quantities for both the scattered pion and the scattered electron, and to positively identify the recoil electron by an array of lead-glass shower detectors. Finally, previous experience with data analysis for πe scattering indicated the importance of obtaining "clean" events—events for which the detector efficiency was high and in which there were no background tracks. To obtain such events the beam logic was designed to eliminate triggers for which there was more than one beam particle.

A layout of the experimental apparatus is shown in Fig. 2. The incident beam was defined by a series of coincidence counters B_0 , B_1 , and B_2 , an anticoincidence counter A_H , and a threshold Čerenkov counter \check{C}_{th} . The four proportional wire chambers (PWC's) in block I (defined in Fig. 2) had fast analog signal outputs which were used as part of the beam signature; they were also used to record the incident-beam trajectories. The scattered particles emerging from the liquid hydrogen (LH_2) target had their trajectories recorded by the block II PWC's before entering the analysis magnets. Four PWC chambers were placed between the two magnets to provide a two-particle signature as part of the trigger requirements. The scattered particles were magnetically deflected in the horizontal plane and an array of spark chambers in block III recorded their trajectories to provide momentum information. Both particles then passed through a trigger hodoscope composed of four plastic scintillators. The electronic logic of this hodoscope required two particles to satisfy its requirements. Next was a lead-glass shower-counter array; its logic required the pulse height of one of the particles to be consistent with that of an electron shower. The last element in the spectrometer was a thick

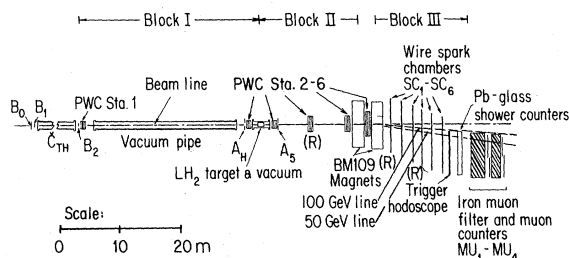


FIG. 2. Schematic layout of the apparatus, showing the three regions of the spectrometer: block I (before the target), block II (after the target, but before the magnet), and block III (after the magnet). R denotes rotated chambers.

two-section iron absorber with scintillation counters placed behind each section to detect the presence of muons. To minimize multiple scattering, extraneous beam interactions, and radiative corrections, a vacuum pipe was used in block I and helium bags were used in blocks II and III.

B. Beam

The experiment was performed in the west branch of the M1 beam line in the meson area at Fermilab. Protons were extracted from the main ring and focused on a beryllium target. Negatively charged secondary particles were selected at an angle of 3.4 mrad with respect to the incident proton beam and transported 440 m to the LH_2 target in the spectrometer.

The beam was tuned to a momentum of 100 GeV/c with $\Delta p/p \approx 0.2\%$ (rms). The transport elements were adjusted to place the third and final focus of the beam at the plane of the trigger hodoscope. The beam spot at the trigger-counter array was ≈ 1 cm²; it was ≈ 2 cm vertically by ≈ 1.5 cm horizontally at the LH_2 target. A detailed description of the M1 beam-transport system is given in Ref. 3.

During the course of the experiment, typically $2-4 \times 10^5$ particles/sec were incident upon the spectrometer. Only about one-third of these particles were defined to be "usable" pions. A usable beam particle required an electronic coincidence among signals from the three plastic scintillation counters B_0 , B_1 , and B_2 , the threshold Čerenkov counter \check{C}_{th} , three of the four PWC's in each of the two stations in block I and the absence of a signal in A_H (an anticoincidence counter used to reject beam outside a 5.1-cm diameter). More than 90% of the beam fit within the defining counters B_1 , B_2 , and A_H . The size of B_0 was made large enough to intercept all beam particles which would pass through our apparatus.

In addition to these requirements, additional

beam logic allowed us to approach electronically a condition of "zero beam intensity" which improved the detector performance by minimizing background tracks in the chambers. A 1- μ sec signal from B_0 was used to form a veto, B_0K , in the beam coincidence and prevented scaling of beam particles or event triggers which had a beam track in the preceding 1 μ sec. A signal from B_1 created a veto, BD , if the pulse height exceeded 1.5 times that of a minimum-ionizing particle. This veto eliminated beam counts or triggers in which there was more than one particle in a given rf bucket. Another signal from B_1 , labeled NBK , was used to veto the beam coincidence when one or more particles appeared in the rf bucket immediately following the initial beam particle.

While the B_0K logic protected the chambers for the 1- μ sec period before an event trigger, the time delay between the triggering particle and the application of high voltage to the spark chambers (≈ 400 nsec) made it possible for extraneous beam particles to pass through the chambers and be detected. We did not veto this class of events, but a circuit was created to monitor these triggers, flag the events, and accumulate a separate set of scalers for beam of this type. Thus, all

events followed by an extra beam particle within 450 nsec after the trigger were flagged and scaled separately. This class of events then had its own beam normalization and was handled separately in the analysis.

The threshold Čerenkov counter \check{C}_{th} was 28 m long and filled with helium gas at 2.7 psi. The counter served to remove kaons and antiprotons from the counted beam, but did not reject the small ($<0.5\%$) muon and electron contamination in the beam.

Each PWC in block I had a fast adder circuit whose output-signal pulse height was proportional to the numbers of hit wires in that plane.⁴ The signals from each of the four planes in station 1 were used in majority logic (3 out of 4) to form the "single-beam" signal SB1 for station 1. Another signal SB2 was similarly formed for station 2. The "double-beam" signal DB1 for station 1 was formed in a similar fashion with the discriminator sensitivities set between that of a single- and double-beam hit with less stringent majority logic (2 out of 4). Another signal DB2 was similarly formed for station 2.

The complete beam logic was

$$\text{BEAM} = B_0 \cdot B_1 \cdot B_2 \cdot \check{C}_{th} \cdot \text{SB1} \cdot \text{SB2} \cdot \overline{(\text{DB1} + \text{DB2})} \cdot \overline{A_H} \cdot \overline{B_0K} \cdot \overline{BD} \cdot \overline{NBK}. \quad (2.1)$$

The beam characteristics were carefully monitored during data taking by eighteen special "beam runs" interspersed with the data runs. Each beam run consisted of 1600 triggers initiated by the beam coincidence. In this manner we continually measured the beam momentum and its spatial and angular characteristics. These measurements of the characteristics of the beam were used as input parameters to calculate various corrections to the data.

C. Liquid-hydrogen target

The LH_2 was contained in a 50-cm-long stainless-steel jacket, 11 cm in diameter. The target area was defined by a 10-cm copper liner which acted as a heat shield to protect the inner region from bubbling. The liquid was contained on each end by 0.03-mm flat mylar windows and the pressure was held by 0.13-mm domed mylar windows filled with hydrogen vapor. The entire target assembly was housed in a vacuum region which extended a total length of roughly 2.5 m along the beam line. A schematic diagram of the target is shown in Fig. 3.

The target-flask pressure was continuously monitored by a Wallace and Tiernan capsule-type gauge (Model No. 62-050) connected to the

top of the flask. The specially designed end windows were flat to within 0.05 mm. This allowed a determination of the product of length times density (ρL) for this target to an accuracy of 0.27%. The total number of atomic electrons per cm^2 in the target (including the H_2 vapor and mylar end windows) was determined to be $(2.1543 \pm 0.0058) \times 10^{24} / \text{cm}^2$. The extended vacuum region, one meter from each end of the target flask, allowed a clean separation of events with vertices originating in the target volume from

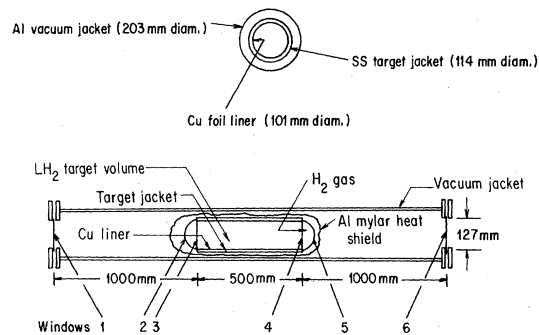


FIG. 3. Details of the liquid-hydrogen target, showing the mylar windows and the vacuum regions upstream and downstream of the hydrogen.

those in the material outside the vacuum region.

To veto strong-interaction events, an anti-coincidence counter A_5 was located 2.5 m downstream from the center of the LH_2 target. This counter had a 10-cm diameter hole centered on the beam to allow πe elastic events to pass through without being vetoed. It was sandwiched between two 6.4-mm-thick aluminum plates and had a 25-mm brass plate mounted on the upstream face with matching holes. The brass and aluminum plates acted as absorbers to reduce vetoes from soft electrons (δ rays) or radiative photons associated with πe scatters. The efficiency of the counter/absorber for low-energy electrons has been studied experimentally and by Monte Carlo methods (see Sec. IIIC 9). Discriminated signals from the top and bottom photomultipliers were logically added to form the A_5 signal which went directly into the master trigger as a veto.

D. Proportional wire chambers

Proportional wire chambers were used as track detectors and provided triggering information in blocks I and II of the spectrometer. In addition, four planes were situated between the two spectrometer magnets for use in the event trigger. The PWC stations consisted of two vertical and two horizontal planes, joined together to form a single physical unit. The wire spacing was 2 mm for all chambers, but the chamber supports were precisely aligned to offset the planes with parallel wires by one-half the wire separation, yielding an effective wire spacing of 1 mm in both the horizontal and vertical directions for tracks of near normal incidence. PWC stations 1, 2, and 3 had active areas of $12.8 \times 12.8 \text{ cm}^2$, stations 4 and 5 had active areas of $25.6 \times 25.6 \text{ cm}^2$, and station 6 had an active area of $35.2 \times 35.2 \text{ cm}^2$. Station 4 was rotated 45° with respect to the horizontal. The gas used was Ar- CO_2 mixed 80%-20% and was continuously flowing through the chambers at a low rate.

Each of the ≈ 2500 sense wires in the system had its own amplifier and logic circuitry. Sense wires with signals in coincidence with a strobe pulse from the fast-logic loaded corresponding shift registers. Each chamber's shift-register outputs were serially read out by a clock pulse after the spark noise subsided. The sense-wire pulse trains, together with an artificial data start pulse and several stop pulses, were digitized in the same manner as the spark chamber data by a Science Accessory Corporation (SAC) Model No. 1148 scaler bin. The SAC scalers were read out by a SAC-CAMAC interface unit residing in a CAMAC crate. A more complete description of

these chambers is contained in Ref. 5.

A PWC two-particle signal TP was derived from signals from station 5 and station 6, and required the presence of two separated particles in block II. These signals were obtained from specially designed circuits whose output was a function of the number of wires that had fired and of their separation. An output from each wire went to three OR circuits in a manner such that two adjacent wires drove a total of four OR's. The outputs from the OR's were summed and the amplitude of the resulting signal was thus determined by the number of wires hit and their separation.⁴ The discriminator thresholds for these signals were set to correspond to at least two hits separated by at least one intervening wire. One vertical (v) and one horizontal (h) plane in each of stations 5 and 6 were equipped with this circuitry. The final two-particle logic signal TP was formed by a coincidence between stations 5 and 6:

$$\text{TP} = (\text{TP}5v + \text{TP}5h) \cdot (\text{TP}6v + \text{TP}6h). \quad (2.2)$$

All chambers were voltage plateaued in the beam at the beginning of the data taking and their efficiencies were continuously monitored by the on-line track-finding programs. A PWC test module was constructed which, upon a signal from the on-line computer, pulsed all planes at the end of the accelerator spill. This test exercised the entire PWC readout system and immediately revealed any electronic malfunction. Calculations from the off-line data analysis showed that all planes were greater than 99% efficient.

E. Spectrometer magnets

Two Fermilab BM109 magnets were used in the spectrometer. They were each 1.8 m long and had vertical apertures of 20 cm and horizontal apertures of 60 cm. Their total field integral of 70 kG m deflected a 100 GeV/c beam particle through an angle of 21 mrad. Particles emerging from the target in the central beam direction with momentum 50 GeV/c were deflected by 42 mrad and defined the "half-energy" line. The midpoint between the two magnets was 15 m downstream from the target and the center line of each magnet was coincident with the half-energy line.

The field of each BM109 was accurately mapped.⁶ The straight-line field integral was measured along the length of each BM109 on a $2.5 \times 2.5 \text{ cm}^2$ grid over their entire length including the fringe fields at both ends. The deviation from the central field integral was no greater than 0.12% for the regions traversed by either a pion or an electron from an elastic-scattering event. These small deviations were taken into account in the algorithm which determined mo-

menta. During the course of the experiment, the BM109 field was monitored by a NMR probe whose value was checked and recorded for each data run. The rms momentum resolution for the scattered particles ranged from 0.08% at 30 GeV/c to 0.3% at 100 GeV/c.

F. Spark chambers

The pion and electron trajectories downstream from the analyzing magnets were recorded by a series of six wire spark chambers spaced equally along a 9-m lever arm. Each chamber provided coordinate information in two orthogonal directions x and y ; the first and third chambers were rotated in the plane of the chamber by $\pm 30^\circ$, respectively, to resolve track ambiguities.

The active area of each chamber was 150×50 cm². The horizontal aperture allowed complete acceptance of the desired pion and electron trajectories as well as calibration tracks taken with the magnets off. Each chamber consisted of two orthogonal wire planes composed of 127 μ m aluminum wires spaced at 1-mm intervals. The gap was 9.1 mm. A 90% neon and 10% helium gas mixture with an admixture of 1% alcohol was employed. The gas was continuously recycled and purified.

The coordinate information was obtained from a magnetostrictive delay line readout (wands). The wand preamplifiers and the discriminator/scaler system were Science Accessory Corporation units. Owing to the small opening angles of the elastic πe events and the lack of momentum dispersion in the vertical or y direction, the y wands were read out at both ends to aid in the detection of closely spaced sparks in this projection. To compensate for signal attenuation along the horizontal or x wands, a threshold ramping unit,⁷ started by the event trigger, decreased the discriminator thresholds at a rate matching the signal attenuation. Each x readout could handle as many as six sparks per event. Each of the two y readouts could record as many as four sparks.

To shorten the recovery time of the chambers, a pulsed clearing field 1.2 kV in amplitude and 5 msec in duration was applied 0.5 msec after an event trigger. The memory time of the chambers was set by a dc clearing field of 40 V. The chambers were plateaued with radioactive sources before the run and their efficiencies were continuously monitored on line by the track-finding programs. They were run with an electronic deadtime of 15 msec during data-taking, although the actual trigger rate was only ≈ 14 per second. During beam runs the deadtime was increased to 30 msec to protect the chambers. The average

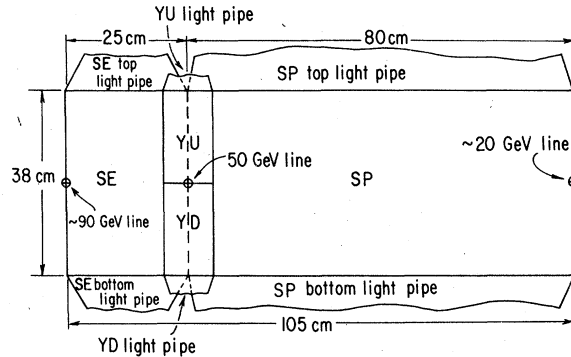


FIG. 4. Beam's-eye view of the scintillation-counter hodoscope array used in the trigger for elastic events. The logic requirement was 2 out of 3, where the 3 logical conditions were SE , SP , and $YU \cdot YD$.

single-chamber efficiency for πe scatters was better than 98%.

G. Target hodoscope

The trigger hodoscope was an array of four plastic scintillators, arranged as shown in Fig. 4. This hodoscope's two-particle signature was

$$SESP = [SE, SP, (YU \cdot YD)]_{2 \text{ of } 3}, \quad (2.3)$$

i.e., the condition was satisfied when any two of the three component signals were present. These SE and SP counters were viewed by photomultipliers at both the bottom and top, and the signals SE and SP were formed from OR's of the signals from the individual photomultipliers. In the simplest two-particle trigger for πe elastic events, only a coincidence between SE and SP which straddle the half-energy line, would have been required. YU and YD would not have been necessary. Because the beam was focused to a small spot, ≈ 1 cm², at the trigger hodoscope, the pion and the electron usually struck the hodoscope on opposite sides of the half-energy line. The YU and YD counters were added to trigger on those infrequent events for which both particles were on the same side of the half-energy line, and also those events for which either the pion or electron went between SE and SP in the finite-sized crack. For each trigger the electronic logic recorded the presence or absence of the output of the discriminator circuit for each photomultiplier tube mounted on the trigger hodoscope. This information was used in the off-line analysis to calculate the efficiencies of each individual scintillation counter (see Sec. III C 7).

H. Lead-glass shower counters

In addition to the stringent kinematic constraints of the elastic-scattering hypothesis, the electron

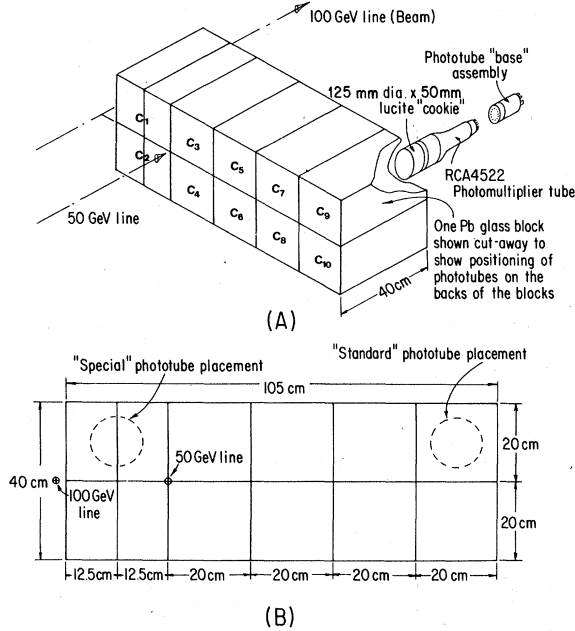


FIG. 5. (a) Isometric view, and (b) beam's-eye view of the lead-glass Čerenkov counters.

was identified by its energy deposition in an array of ten lead-glass shower counters just downstream of the trigger hodoscope. The ten counters were arranged in two rows, above and below the median plane, as shown in Fig. 5. Eight of the counters were to the low-momentum side of the half-energy line and the remaining two counters were to the high-momentum side of this line. The eight counters on the low-momentum side were constructed of $20 \times 20 \times 40$ cm³ blocks of lead glass; the two counters on the high-momentum side were each constructed of two $12.5 \times 20 \times 40$ cm³ blocks. All blocks were Schott SF-2 glass (PEMG1), polished on all sides. The counter blocks were placed with their longest dimension (40 cm) parallel to the half-energy line and were optically isolated by layers of aluminized mylar. Each counter was viewed at the center of its downstream face by a 12.7-cm RCA 4522 photomultiplier tube which was optically coupled to the block by a lucite adaptor and silicon grease which permitted a magnetic shield to extend beyond the photocathode surface.

An electron signature, determined by pulse height correlated with position, was required from the lead-glass shower-counter array. The correlation between a particle's position in the horizontal plane downstream of the analyzing magnets and its energy meant that each vertical edge in the shower-counter array corresponded to a unique range of electron energies. A pulse-

height requirement based on the minimum energy seen in each block was constructed. To avoid biases or trigger inefficiencies, the pulses from the counters were first summed in groups of four: the sums were labeled

$$\begin{aligned} C_A &= C_1 + C_2 + C_3 + C_4, & C_B &= C_3 + C_4 + C_5 + C_6 \\ C_C &= C_5 + C_6 + C_7 + C_8, & C_D &= C_7 + C_8 + C_9 + C_{10} \end{aligned} \quad (2.4)$$

As can be seen in Fig. 5, these sums represent physically overlapping groups of counters (e.g., counters C_3 and C_4 appear in C_A and C_B , representing the lower-energy part of the former and the higher-energy part of the latter group). The thresholds for each group of four was set close to the minimum energy expected in the group without introducing inefficiencies in the trigger. As an example, the C_A threshold was set to the minimum energy corresponding to an event at the low-energy edge of counter C_3 or C_4 . A shower developing near this edge and losing energy into counters C_5 and C_6 would not deposit sufficient energy in the counters of the C_A sum to exceed that threshold but would be well above the threshold for the C_B sum which was determined by the C_5 and C_6 edge. The final shower-counter signal used in the event trigger was the logical OR:

$$C = C_A + C_B + C_C + C_D. \quad (2.5)$$

The use of shower counters in the event trigger required precise calibration and balancing of all photomultiplier gains in the system. To accomplish this, a 35-GeV/c electron beam was steered into each counter. The gains were adjusted so that for πe events the minimum-energy electron entering each counter would give the same pulse height. This procedure allowed one threshold setting for all discriminators. Separate data runs were taken with the lead-glass counter-array signal removed from the trigger so that the presence or absence of the signal in coincidence with the remaining event trigger could be studied.

The modularity of the system allowed correlation of the spark-chamber track information with the shower-counter pulse heights. The track of an electron candidate was traced to the shower-counter array and the momentum measured in the spectrometer was compared to the energy deposited in the appropriate counter(s). The normalized pulse height, defined to be the ratio of shower energy to the corresponding spectrometer particle momentum, was used to further aid in discrimination of background events from elastic scatters. The resolution of the system determined from the rms width of the normalized pulse-height peak for all elastic events was $\approx 6\%$. It is shown in Fig. 6.

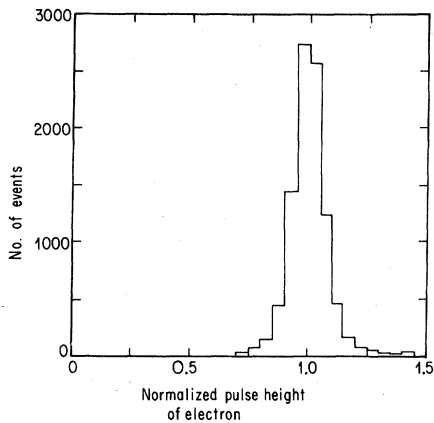


FIG. 6. Distribution of the ratio of the measured electron energy in the lead-glass shower counters to the measured electron momentum in the spectrometer for events satisfying elastic kinematics.

I. Muon identifier

A 3.75-m iron filter, located just downstream of the shower-counter array, was used to identify muons which had elastically scattered from electrons in the target. The filter was divided into two segments, each of which was followed by plastic scintillators. The first segment was 2.5 m long, $80 \times 180 \text{ cm}^2$ in cross section, and the second segment was 1.25 m long and of similar cross-sectional area. Each scintillator was $1.25 \times 76 \times 71 \text{ cm}^3$ and was viewed by a single photomultiplier. The counters were overlapped in a manner to cover the area of interest while remaining within the shadow of the iron filter. Information from the four counters was recorded for each event and used in the off-line analysis to identify candidates for μe scatters.

J. Event trigger and data taking

The requirements for an event trigger were a BEAM signal from the beam-monitor circuits, a two-particle signal from the trigger hodoscope *SESP*, a shower counter signal *C*, a two-particle signal from the PWC's between the analyzing magnets TP, and no signal in the anticoincidence counter \bar{A}_5 . The electronic logic for the master trigger was

$$\text{MASTER} = \text{BEAM} \cdot \text{SE SP} \cdot C \cdot \text{TP} \cdot \bar{A}_5. \quad (2.6)$$

When the conditions for an event trigger had been met, the MASTER trigger pulse which was formed activated various gates, applied a load pulse to the PWC's, fired the spark chamber high-voltage pulsers, and began the data acquisition processes. The data acquisition was controlled by the on-line computer, a Hewlett-

Packard model 2100, through a branch driver which decoded the computer commands and implemented them in signals according to the CAMAC conventions.

For the duration of a spill ($\approx 1 \text{ sec}$) data transferred to the computer were stored on the disk. At the end of the accelerator spill, the computer activated two calibration tests employing light pulses to the lead-glass shower counters and PWC test pulses. Data were then transferred from the disk onto magnetic tape and an on-line analysis mode was initiated.

The time between spills ($\approx 10 \text{ sec}$) allowed the computer to analyze a large portion of the data. It decoded and histogrammed chamber and counter information, accumulated scaler counts, analyzed the calibration tests, provided a detailed display of event topology, and performed simple track finding and πe event selection. The track-finding information was used to determine spark- and proportional-chamber efficiencies and to provide on-line momentum analysis.

Over a period of two weeks, 24 normal data runs were taken with typically 21000 triggers each. In addition five target-empty runs of 6000 triggers each were taken with liquid hydrogen removed from the target leaving only residual hydrogen gas. There were also three "straight-through" runs of typically 5000 triggers each which required a beam trigger, but with the spectrometer magnets run down to zero current (and zero measured residual field). These runs provided straight tracks through the entire spectrometer for chamber alignment, which was necessary for the absolute calibration of the incident-beam momentum.

III. ANALYSIS OF THE DATA

The data were analyzed in four steps: (1) reconstruction of the events from the raw data, (2) kinematic selection of πe elastic events using a χ^2 fitting procedure, (3) corrections to the data, and (4) determination of the pion form factors.

A. Event reconstruction

The event-finding programs BEST and VAL used conventional techniques to find tracks in wire chambers. In each block and in each view perpendicular to the beam direction, a set of sparks hypothesized to lie on a straight line was fitted by a least-squares method. In the reconstruction rotated chambers were used to resolve ambiguities in projections. All chambers were aligned in a coordinate system by means of beam particles which traversed all chambers with the magnetic field turned off.

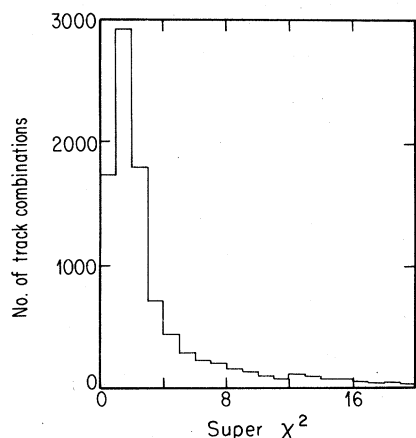


FIG. 7. Super χ^2 per degree of freedom used in the selection of elastic candidates in the event-finding program BEST.

The event-finding program forms all combinations of tracks in an event which may satisfy the elastic topology of $\pi^- + e^- \rightarrow \pi^- + e^-$. For each set of tracks, the following were calculated: (1) the χ^2 for the line fit to each track, (2) a vertex χ^2 for the intersection at a point in the target of the incoming track and the two outgoing tracks in both views, and (3) a magnet-match χ^2 for the intersection at the magnet center of both entering and exiting tracks. These χ^2 's were summed

$$\chi_{\text{super}}^2 = \sum_{\text{tracks}} \chi_i^2 + \sum_{\text{target}} \chi_i^2 + \sum_{\text{magnet}} \chi_i^2 \quad (3.1)$$

for each combination of tracks, and the set of tracks with minimum super χ^2 was chosen as the most probable combination. A typical distribution of χ_{super}^2 is shown in Fig. 7. As an indicator of the geometrical precision of the reconstruction, the fitted vertex position for both full- and empty-target runs are displayed in Figs. 8(a) and 8(b).

B. Kinematic event selection

The elastic-event selection employed four criteria: (1) a lead-glass shower-counter measurement of the electron energy, (2) a constrained χ^2 fit of the spectrometer measurements to the reaction hypothesis



(3) a subsequent cut on the fitted bremsstrahlung photon energy at $E_\gamma \leq 4.0$ GeV, and (4) a geometry cut on the vertex position in the target. These selection criteria were sufficient to reduce the hadronic background to less than 1% of the πe elastic signal over the full q^2 range.

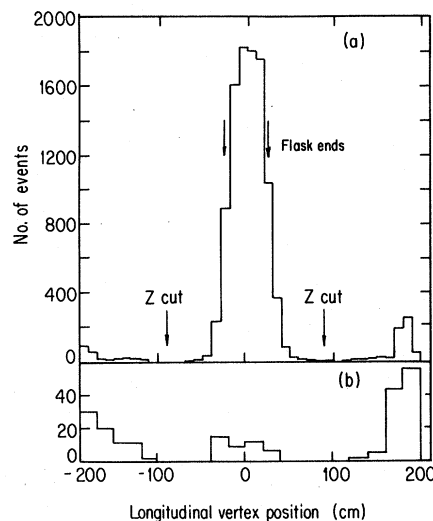


FIG. 8. (a) The distribution of geometrically reconstructed vertex locations for selected elastic-scattering events. The target is centered at $z = 0$, and the upstream and downstream vertex cuts are noted. (b) The distribution of vertex locations of selected elastic events during target-empty running. The small number of events in the target region is consistent with the expected amount of hydrogen vapor in the target volume.

1. Lead-glass shower counters

The energy of the recoil particle was measured in an array of ten lead-glass shower counters each of 14 radiation lengths located behind the trigger-counter array. Corrections were made for shower sharing among the counter modules and for losses from the rear of the counters ($\approx 5\%$ at the highest energy). The distribution of the ratio of measured shower energy to measured spectrometer momentum is shown in Fig. 6. A cut was made on this distribution at one-half of the expected energy for the electron track.

2. Constrained χ^2 fit

Events with elastic topology were subjected to a constrained χ^2 fit⁸ to the elastic- πe -reaction hypothesis with the addition of a bremsstrahlung photon from the recoil electron traversing the spectrometer matter. The least-squares fitting procedure, a program called FIT, found the best set of fitted momenta which satisfied energy-momentum conservation exactly and at the same time coincided with the measurements. We used χ^2 at the 10^{-6} confidence level to cut the data.

The four energy-momentum equations are

$$P_{x1} = P_{x2} + P_{x3} + P_{x4}, \quad (3.3)$$

$$P_{y1} = P_{y2} + P_{y3} + P_{y4}, \quad (3.4)$$

$$P_{z1} = P_{z2} + P_{z3} + P_{z4}, \quad (3.5)$$

$$E_1 + m_e = E_2 + E_3 + E_4, \quad (3.6)$$

where particle 1 is the incident pion, particle 2 is the scattered pion, particle 3 the scattered electron, and particle 4 the bremsstrahlung photon. Equation (3.6) is numerically similar to Eq. (3.5) due to the small transverse momenta available when scattering from a relatively low-mass target, in this case, the electron. Those equations are not equivalent, however, and the energy equation may be cast into a more useful form by

$$\frac{P_{x1}^2 + P_{y1}^2 + m_\pi^2}{P_{z1}} + 2m_e \approx \frac{P_{x2}^2 + P_{y2}^2 + m_\pi^2}{P_{z2}} + \frac{P_{x3}^2 + P_{y3}^2 + m_e^2}{P_{z3}} + \frac{P_{x3}^2 + P_{y3}^2}{P_{z3}} \frac{E_4}{P_{z3}}, \quad (3.8)$$

which is the algebraic energy-constraint equation used in the fitting procedure. The bremsstrahlung-photon energy was the only free parameter in the fit, since its direction was constrained to be along the direction of the recoil electron.

The algebraic procedure employed to minimize χ^2 and to satisfy the constraint equations is that given in Ref. 8. Let \underline{x} be the vector of n fitted parameters. Since there are three particles, each with three momentum components, and one bremsstrahlung photon fixed along the direction of the scattered electron, $n=10$. Let \underline{f} be the vector of k constraint equations in the form $\underline{f}=0$, $k=4$ corresponding to the four equations of momentum-energy conservation. Let \underline{m} be the vector of n kinematic measurements, and \underline{G}^{-1} be the $n \times n$ error matrix on these measurements. (The bremsstrahlung photon is treated as an unmeasured variable and assigned a weight of zero. See

expanding Eq. (3.6) to first order in $(P_x^2 + P_y^2 + m^2)/P_z^2 \approx 10^{-4}$, and then subtracting out the longitudinal-momentum constraint Eq. (3.5). Approximating each energy term in Eq. (3.6) as

$$E = (P_x^2 + P_y^2 + P_z^2 + m^2)^{1/2} \\ = P_z + \frac{P_x^2 + P_y^2 + m^2}{2P_z} + \dots \quad (3.7)$$

and subtracting Eq. (3.5), Eq. (3.6) becomes

Ref. 8 for details.) χ^2 is defined as

$$\chi^2 = (\underline{x} - \underline{m})^t \underline{G} (\underline{x} - \underline{m}). \quad (3.9)$$

To minimize Eq. (3.9) and satisfy the constraints, the quantity

$$M = \chi^2 + 2\underline{\alpha} \cdot \underline{f} \quad (3.10)$$

is formed where $\underline{\alpha}$ is a vector of k Lagrange multipliers. Setting the derivatives of M with respect to the n parameters and the k Lagrange multipliers to zero yields $(n+k)$ equations in $(n+k)$ unknowns. The energy constraint, Eq. (3.8), is not linear in the parameters, but it may be easily expanded to first order in \underline{x} , whereupon the $(n+k)$ linear equations are solved. If this solution did not satisfy the constraint equations to sufficient numerical precision (10 keV in this case), the procedure was repeated using the

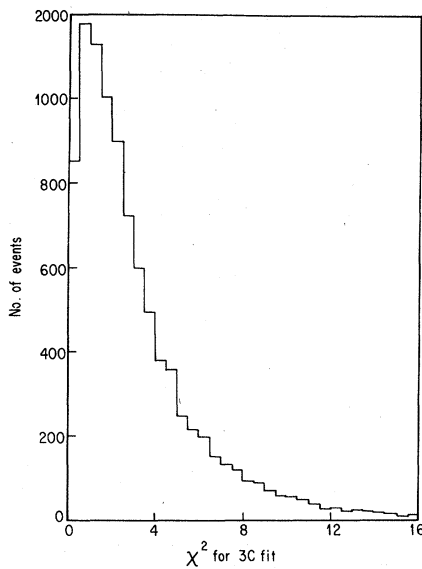


FIG. 9. Kinematic event χ^2 for the three-constraint fit to πe elastic scattering.

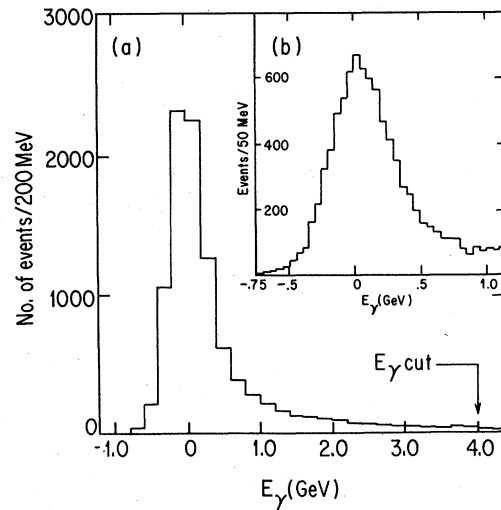


FIG. 10. (a) The distribution of fitted bremsstrahlung-photon energies in the kinematic fit. The cut applied to the data was at 4.0 GeV. (b) The same distribution, but near zero bremsstrahlung energy. The width of the distribution is dominated by the beam momentum spread.

TABLE I. Corrections to the data.

Effect	Correction (%) \pm error (%)
q^2 -independent corrections	
1. Event-finding inefficiencies	0.91 ± 0.54
2. Trigger inefficiencies	0.12 ± 0.45
3. Target electron density	0.00 ± 0.27
4. μ^- , e^- , K^- , \bar{p} contaminations	0.40 ± 0.20
5. Beam cut	2.70 ± 0.12
6. Secondary π attenuation	4.71 ± 0.10
7. Primary π decay, attenuation	3.06 ± 0.07
8. δ rays in A_5	0.39 ± 0.04
The range of the q^2 -dependent corrections and their average errors	
1. Target and spectrometer bremsstrahlung	$(17.4-26.8) \pm 0.5$
2. πe radiative corrections to order α^3	$(7.3-8.8) \pm 0.4$
3. Hadronic background	$(0.1-0.9) \pm 0.4$
4. μe background	$(0.0-0.5) \pm 0.2$
5. Geometrical inefficiency	$(0.6-4.7) \pm 0.1$
6. Secondary π decay	$(0.4-1.1) \pm 0.1$

fitted values as input to the next iteration. The three-constraint χ^2 distribution is shown in Fig. 9.

3. Bremsstrahlung photon

The fitted bremsstrahlung-photon energy spectrum is displayed in Fig. 10, showing the peaking near zero photon energy and the radiative tail. The width of the peak is dominated by the pri-

TABLE II. q^2 -dependent corrections to $|F_\pi(q^2)|^2$ as a function of q^2 . The q^2 bins are those used in the presentation of the results for $|F_\pi(q^2)|^2$ in Table IV, the numbering of the corrections coincides with the labeling in Table I.

q^2 [(GeV/c) 2]	Correction (%)					
	1	2	3	4	5	6
0.0317	17.4	7.29	0.05	0.31	4.69	0.43
0.0337	18.1	7.74	0.00	0.35	1.46	0.45
0.0358	18.7	7.97	0.00	0.41	0.75	0.46
0.0378	19.2	8.08	0.14	0.45	0.60	0.47
0.0399	19.7	8.17	0.00	0.45	0.78	0.48
0.0419	20.1	8.23	0.00	0.46	1.36	0.49
0.0439	20.6	8.28	0.00	0.47	2.55	0.51
0.0460	21.0	8.32	0.15	0.45	1.29	0.52
0.0480	21.4	8.36	0.00	0.44	1.14	0.54
0.0501	21.8	8.40	0.18	0.35	1.14	0.54
0.0521	22.3	8.44	0.20	0.12	1.13	0.55
0.0542	22.7	8.48	0.25	0.02	1.15	0.58
0.0562	23.1	8.51	0.36	0.00	1.48	0.66
0.0583	23.6	8.55	0.39	0.00	4.03	0.67
0.0603	24.0	8.59	0.85	0.00	0.89	0.71
0.0623	24.5	8.62	0.45	0.00	0.58	0.76
0.0644	25.0	8.66	0.61	0.00	0.56	0.84
0.0664	25.6	8.70	0.00	0.00	0.58	0.87
0.0685	26.2	8.74	0.90	0.00	0.56	1.09
0.0705	26.8	8.77	0.00	0.00	0.59	1.01

mary-beam momentum spread. A cut in fitted photon energy was made at 4.0 GeV, where the spectrum is nearly flat.

4. Target vertex

All events were required to satisfy a vertex-geometry cut about the target as indicated in Fig. 8(a). Because of the clean separation between events from the liquid hydrogen and from other sources, no correction was required for this cut.

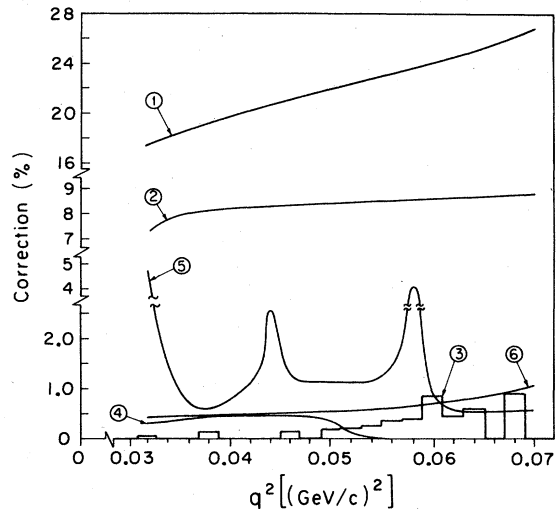


FIG. 11. The six q^2 -dependent corrections to the cross section $d\sigma/dq^2$ expressed as a percent increase of the cross section. The corrections are (1) target and spectrometer bremsstrahlung, (2) πe radiative corrections, (3) hadronic background, (4) μe background, (5) geometrical inefficiency, and (6) secondary π decay.

C. Corrections to the data

All corrections to the data are listed in Table I and are grouped according to whether they are q^2 dependent or q^2 independent. For the six q^2 -dependent corrections we also list the correction to the square of the form factor for each q^2 bin in Table II. The q^2 dependence of these six corrections is shown graphically in Fig. 11. The errors listed in Table I are the total errors contributed by each correction. In the case of the q^2 -dependent errors they are average total errors.

Some effects are listed for which there is no correction; they have been included because they contribute to the error. Some of the q^2 -independent corrections could be regarded as q^2 dependent in principle, but they have been grouped with q^2 -independent corrections because no significant q^2 -dependent effects were uncovered in their calculation. The corrections for the attenuation of the scattered pion (secondary-pion attenuation), δ rays in A_5 , event-finding inefficiencies, and TP inefficiencies fall into this category. The remainder of this section is devoted to a detailed discussion of the corrections in Table I.

1. Beam analysis and corrections

Because the size, angular divergence, and momentum dispersion of the incident beam enters into the measurement of the pion form factor in

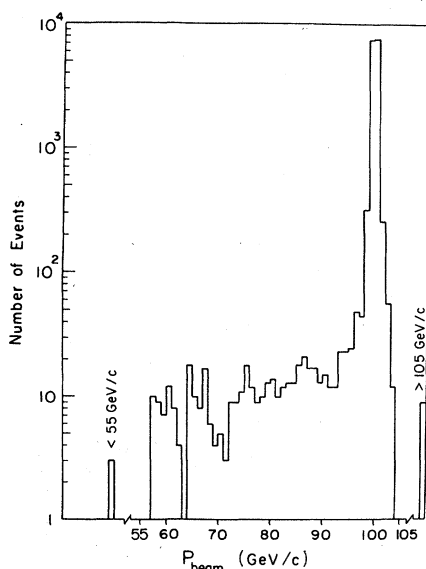


FIG. 12. The momentum spectrum of the incident π^- beam from the sample of beam events used as input to the various beam-dependent Monte Carlo calculations. This spectrum was used to determine the beam scaler correction for beam particles outside the interval ($P_{\text{beam}} - 4 \text{ GeV}/c$) to ($P_{\text{beam}} + 4 \text{ GeV}/c$).

several ways, special beam runs were taken at regular intervals throughout the running using only the beam part of the πe trigger. Figure 12 shows a momentum distribution of beam particles. These runs were analyzed, and a sample of measured and geometrically reconstructed beam tracks were used as input to the Monte Carlo calculation of geometric efficiency, event-finding efficiency, and radiative corrections.

The data shown in Fig. 12 were also used to determine the correction for the number of beam particles registered in the beam scalers not falling in the interval ($P_{\text{beam}} - 4 \text{ GeV}/c$) to ($P_{\text{beam}} + 4 \text{ GeV}/c$). These off-momentum beam particles cannot give rise to πe events which would survive the cut on radiated bremsstrahlung-photon energy at 4.0 GeV. This correction also included off-momentum muon contamination from pion decays upstream of the hydrogen target. The total correction for off-momentum beam particles was $(2.70 \pm 0.12)\%$.

The corrections for μ^- , e^- , K^- , and \bar{p} components in the incident beam inside the momentum acceptance are $(0.35 \pm 0.20)\%$ for μ^- , $(0.05 \pm 0.03)\%$ for e^- , and are negligible for K^- and \bar{p} . These numbers were based on an analysis of μe and ee events in the data as discussed in the section on background corrections. There was no correction for K^- or \bar{p} contamination because a threshold Čerenkov counter, which was located in the incident beam and operated below the K^- and \bar{p} thresholds, was required in the beam scaling logic.

The need for a beam-associated-accidentals correction was eliminated by taking advantage of the rf structure in the incident beam coupled with the various kills in the beam scaling logic, as discussed in Sec. II B.

2. Event-finding corrections

An accurate determination of the event-finding inefficiency was made through a combination of three different techniques: (1) a Monte Carlo generation of events, (2) a detailed comparison of the track-reconstruction results from πe -scattering data of two independent event-reconstruction programs VAL and BEST having different track-

TABLE III. Event-finding corrections.

Method	Correction (%) \pm error (%)
MIMIC	0.47 ± 0.10
Comparison of VAL and BEST	0.19 ± 0.19
Perturbations of BEST	0.25 ± 0.25
Combined result	0.91 ± 0.54

reconstruction algorithms and, (3) a detailed series of perturbations of the cuts used in **BEST** carried out on a small sample of data in a search for previously unfound events. In comparing the results of these three techniques we attempted to identify components of the correction which would not have been found by the other two methods. The resultant correction from each method along with the combined result is shown in Table III. Since the result for each technique represents an exclusive component of the correction, we have added them to get the combined result. We have added the errors rather than combining them in quadrature to get a rms value of the error.

The Monte Carlo generation of events was designed principally to determine the effects of various experimental resolutions and efficiencies on the absolute event-finding efficiency of the event-reconstruction program **BEST** and the subsequent kinematic-fitting program **FIT** described above. The loss of events through radiative effects is also dependent on experimental resolution, but these effects were reserved for the radiative-correction calculation which was done in a separate program. The generated events used the spatial resolutions and efficiencies of the PWC's and spark chambers determined from the data. These events included the effect of multiple Coulomb scattering and residual chamber backgrounds determined from the data. The generated events were analyzed by **BEST** and **FIT** and the percentage of events failing either **BEST** or the confidence-level test in **FIT** at the 10^{-6} level was determined. Essentially all the generated events passed **BEST**. Thus, the correction as determined by this procedure is a correction for a loss of events due to experimental resolutions. As shown in Table III the correction is $(0.47 \pm 0.10)\%$. The error includes the systematic uncertainty in our knowledge of the various experimental resolutions.

The VAL-**BEST** comparison and the many perturbations to **BEST** itself were a means of trying to find further residual inefficiencies associated with the track-reconstruction procedures. The fact that very few additional events were found, plus the knowledge that essentially all Monte Carlo-generated events passed **BEST** and only failed at the **FIT** level, gives us confidence in the final event-finding correction. Our best estimate of the event-finding inefficiency is $(0.91 \pm 0.54)\%$.

3. Radiative corrections

The corrections for radiative effects were divided into two parts: (1) a correction for real bremsstrahlung by the recoiling electron from

matter in the liquid-hydrogen target and spectrometer matter and (2) a radiative correction δ , calculated to order α^3 , arising from higher-order scattering diagrams to the πe -event vertex. The calculation was based on straightforward modifications of a Monte Carlo program used in an earlier experiment.⁹

The material contributing to the real-bremsstrahlung correction consisted of 0.056 88 radiation lengths from liquid hydrogen and 0.035 40 radiation lengths from additional material in the spectrometer. The $\pm 0.5\%$ error in this correction is dominated by the uncertainty in the number of radiation lengths of material in the spectrometer. No uncertainty was assigned to the calculational method itself which was based on the work of Tsai.¹⁰ For the radiative correction δ , the systematic error was estimated to be $\delta^2/2$ or $\pm 0.3\%$.¹¹ Coupled with the statistical error from the Monte Carlo calculation, the total rms error is $\pm 0.4\%$.

4. Background corrections

Background subtractions from the πe -event sample were made for μe and hadronic events. The correction for ee events was found to be negligible. The analysis of the μe and ee events detected by our apparatus was used to determine

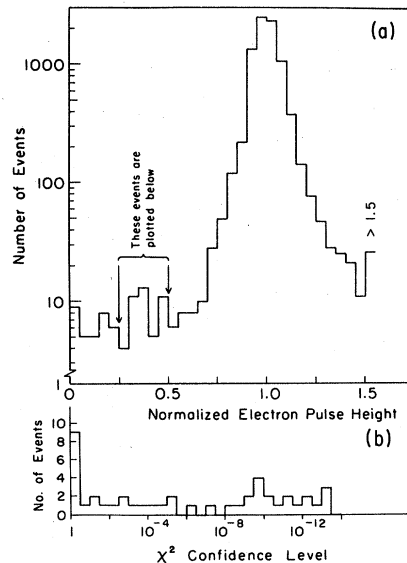


FIG. 13. (a) Normalized pulse height for particles kinematically identified as electrons by **FIT** with a χ^2 confidence level $\geq 10^{-14}$ for the πe -event hypothesis. Electrons have a pulse height of one on this scale. (b) Distribution of events in confidence level between the arrows in (a) or with normalized pulse height between 0.25 and 0.50. The peak at very large confidence level is interpreted as a residual inefficiency in the electron-shower detector while the flat distribution of events at small confidence level is interpreted as hadronic background.

the beam scaling corrections for muon and electron beam contaminations discussed in Sec. III C 1.

The need for a small q^2 -dependent correction to the πe -event sample for residual hadronic background which survived the πe -scattering confidence-level test in FIT can be seen in Figs. 13(a) and 13(b). In Fig. 13(a) we plot the distribution of the ratio of measured lead-glass shower energy to measured spectrometer momentum (normalized lead-glass shower counter pulse height) for particles kinematically identified as electrons by FIT with a χ^2 confidence level greater than 10^{-14} . Figure 13(b) shows a confidence-level distribution for those events in Fig. 13(a) with a ratio between 0.25 and 0.50. The distribution is quite flat apart from a small peak at very large confidence levels. We interpret the peak as a small electron shower detection inefficiency which is discussed below in the section on trigger corrections. The flat part of Fig. 13(b) we interpret as hadronic events. This background must be extrapolated under the electron peak in Fig. 13(a) (normalized electron pulse height greater than 0.5) in a q^2 -dependent manner for events with a confidence level greater than 10^{-6} in order to determine the correct background subtraction.

In Fig. 14 is plotted the normalized lead-glass shower-counter pulse height for a sample of very bad events (confidence level less than 10^{-14}). There is still an electron signal from πe events but the background is greatly magnified over that in Fig. 13(a). The falloff of the data at low shower energy results from the trigger threshold requirement on the shower counters. The solid black curve labeled π shape was taken from a distribution of normalized pion pulse heights from good πe events. The π shape curve has been normalized to the data in the region of area B where there are no threshold effects. The ratios of areas B+C (electron pulse height greater than 0.5) to area A (electron pulse height between 0.25 and 0.5) is 0.71. Therefore, by counting the number of events at any given q^2 with normalized electron pulse height between 0.25 and 0.50 we estimated the number of events to be subtracted from the final πe sample (which requires the normalized lead-glass shower-counter pulse height to be greater than 0.5) by multiplying by 0.71. The results are shown in Table II. Since the extrapolation yielded a correction of one or two events per q^2 bin, the error is of the same size as the correction.

The fraction of muons in the incident beam in the momentum interval ($P_{\text{beam}} - 4 \text{ GeV}/c$) to ($P_{\text{beam}} + 4 \text{ GeV}/c$) was determined as follows. A

sample of 12 000 event candidates reconstructed by BEST was analyzed by the program FIT under the hypothesis that the events were μe rather than πe scatters. The particle identified kinematically as a muon was also required to have triggered at least one counter in the muon filter. The number of incident muons was then determined from the known μe -scattering cross section and a calculation of the geometrical acceptance of the apparatus for μe events. The fraction of muons in the incident beam within the beam momentum cut was $(0.35 \pm 0.20)\%$. The error includes both the statistical error ($\approx 0.10\%$) in the identified sample of μe events and systematic errors ($\approx 0.17\%$) estimated from the spread in values resulting from a choice of different q^2 ranges in the analysis.

The q^2 -dependent subtraction for μe -event background was determined by a Monte Carlo calculation using the muon beam contamination as a normalization factor. A sample of μe events was generated by MIMIC using the real acceptance and experimental resolutions. The events were reconstructed and analyzed by FIT under the same πe -scattering hypothesis used in the actual data analysis. The resulting q^2 -dependent event survival probabilities for μe events together with the ratio of the μe - and πe -scattering cross sections and geometrical acceptances were then used to determine the μe background subtraction displayed in Table II. The absence of μe background in the higher q^2 bins results from the fact that in this region μe and πe events can be kinematically

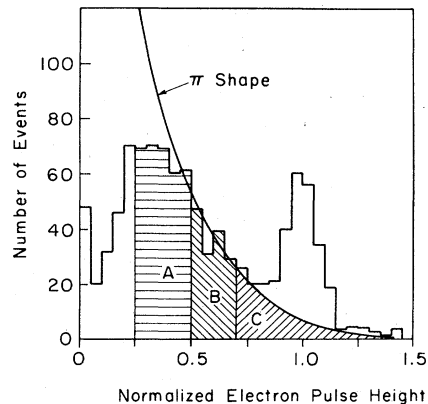


FIG. 14. Normalized pulse height for particles kinematically identified as electrons by FIT with a very poor χ^2 confidence level (C. L. $< 10^{-14}$) for the πe -event hypothesis. These events are primarily hadronic background. The curve labeled π shape is taken from a distribution of normalized pion pulse heights for good πe events and is normalized to the data in region B. The ratio of areas B+C to area A gives a necessary factor in subtracting the hadronic background in the final data sample.

distinguished.

The analysis of the electron contamination in the incident beam is analogous to that for muons. Only a few questionable ee scattering events were found and since the number of electrons in the incident beam was very small ($0.05 \pm 0.03\%$) the ee background subtraction was neglected.

5. Target corrections

There were no corrections to the πe cross sections for target density effects or reconstructed vertex cuts along the incident beam. In computing the number of target electrons, we included the electrons from the mylar and windows of the target flask as well as the hydrogen gas in the dome caps of the flask. Measurements of empty target scattering were consistent with these calculations. The estimated uncertainty in target length was $\pm 0.27\%$.

6. Pion absorption and decay corrections

The absorption or decay of the incident (primary) beam pion was treated as a correction to the incident-beam count, while the absorption or decay of the scattered (secondary) pion was treated as a correction to the πe data. Only the secondary-pion decay correction was significantly q^2 dependent.

Pion-absorption corrections were calculated using the known amounts of material in the spectrometer and hydrogen target together with the π -nucleus cross-section data.¹² In utilizing these data, an effective cross section $\sigma_{\text{eff}} = \sigma_{\text{absorption}} + \epsilon \sigma_{\text{coherent}}$ was used. The parameter ϵ is ≤ 1 , and was estimated using the assumption that a pion elastically scattered by more than 0.5 mrad would cause the loss of the event. The corrections are $(2.90 \pm 0.10)\%$ for the primary pion and $(4.71 \pm 0.20)\%$ for the secondary pion. Although the correction for the secondary pion is q^2 dependent in principle, the dependence was very small and was neglected. The liquid hydrogen contributes 2.59% to the correction for both the primary and secondary pions.

The correction for the decay of the primary pion is already largely included in the beam cut correction for beam particles outside the momentum acceptance. However, there is a small residual correction due to pion decay in block I of the apparatus. Pions which decay in block I have a "kink" in their trajectories of ≤ 0.4 mrad and may be eliminated from the beam analysis by a cut which requires the block I and II slope measurements of the incident beam particle to agree within 0.2 mrad. The residual correction for this cut was calculated to be $(0.16 \pm 0.05)\%$. Thus, the final correction for the absorption or

decay of the incident-beam pion shown in Table I is $(3.06 \pm 0.07)\%$.

The q^2 -dependent correction for the decay of the secondary pion was calculated by using Monte Carlo-generated events from MIMIC which were allowed to decay in the spectrometer. These Monte Carlo events were then analyzed by BEST and FIT, and the q^2 -dependent event loss corrections determined.

7. Inefficiencies in the experimental trigger

The correction for inefficiencies in the πe -event trigger is 0.12%, which results from inefficiencies in the three basic components of the trigger logic: (1) a two-particle signal $SESP$ from a scintillation-counter hodoscope in block III, (2) a signal C above threshold from the lead-glass shower-counter array in block III, and (3) a signal TP from the two-particle PWC logic in stations 5 and 6.

The scintillation-counter signals were recorded for each event. The presence of two phototube signals in logical OR from both the SE and SP counters provided considerable redundancy in the available information. By a suitable choice of event topologies, determinations of the SE , SP , YU , and YD efficiencies were made. Monte Carlo studies using these efficiencies indicate that no correction was required. We have assigned a $\pm 0.1\%$ normalization error for this 0.0% correction.

We have interpreted the small peak in Fig. 13(b) at large confidence level as electrons from πe events with small pulse height. The number of events above background is 7.6. These events were cut from the final data sample because of their low lead-glass shower energy. There were probably some additional events lost because of the threshold setting on the shower-counter pulse height in the trigger. By comparing the π shape with data in Fig. 14 in the region of normalized pulse height between 0.25 and 0.50, we estimated the trigger inefficiency in this region to be $(22 \pm 5)\%$. Combining the trigger inefficiency with the loss from the analysis due to the requirement that the normalized lead-glass shower-counter pulse height be greater than 0.5, we estimated the correction for lost πe events because of the lead-glass shower-counter pulse-height requirement to be $(0.12 \pm 0.15)\%$.

The correction for the inefficiency of the two-particle PWC trigger TP in stations 5 and 6 was determined from the data. πe data were taken without the two-particle requirement in the event trigger logic while recording the presence or absence of the TP signal. An analysis of the data yielded no misses in 267 reconstructed pairs,

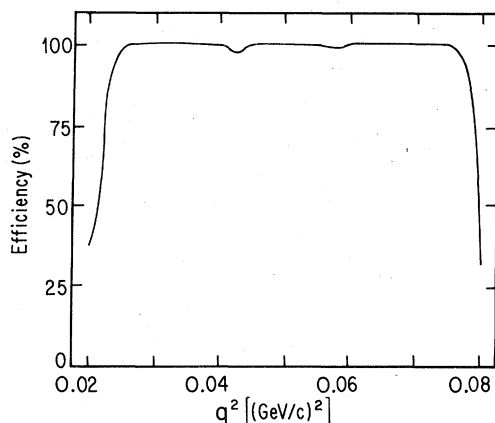


FIG. 15. The geometric efficiency of the spectrometer as a function of the q^2 of elastic events.

or a correction of $(0 \pm 0.43)\%$ at the 68% confidence level.

8. Geometrical acceptance

The geometrical acceptance of the spectrometer was close to 100% over the q^2 range of the data presented and only a small correction was required. The correction was calculated by Monte Carlo methods using the measured experimental geometry and the beam phase space as determined by the beam analysis discussed earlier. The geometrical acceptance is shown explicitly in Fig. 15. Fiducial cuts of 0.5 cm inside the physical edges of the scintillation counters used in the event trigger were made both in the data

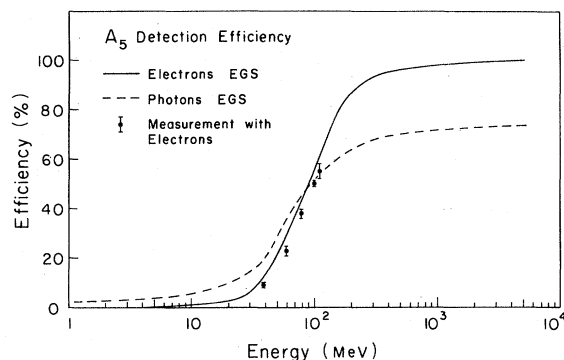


FIG. 16. Detection efficiency of the anticoincidence counter A_5 for electrons and photons as a function of energy. The solid curve is for electrons and the dashed curve is for photons as calculated by a microscopic-shower-development program EGS. The data points represent measurements with low-energy electrons. Both the data and the calculations include the effects of 1.72 radiation lengths of absorber located in front of the counter. Our form-factor results are not sensitive to the slight discrepancy between the measurements and the EGS result.

and the calculation of the geometrical acceptance. Our form factor results are insensitive to variations in these fiducial cuts. We have assigned an uncertainty of $\pm 0.1\%$ to this correction.

9. Anticoincidence corrections

There are two corrections arising from the anticoincidence counter A_5 following the hydrogen target: (1) a correction for target associated δ rays produced by either the incident-beam pion, the recoiling pion, or the recoiling electron which registers in A_5 and vetoes, the event; (2) a correction for hard photons from the πe vertex which registers in A_5 (hard photons generated by bremsstrahlung from the target protons are too forward peaked to contribute to this correction). The second correction is a part of the radiative correction to order α^3 and is not shown explicitly in Table I. An attempt was made to minimize the δ -ray correction by placing an absorber (1.72 radiation lengths) in front of the A_5 scintillator (see Sec. II C). Since both the counter and the absorber had a 10-cm-diameter hole for the recoiling πe pair, δ rays or hard photons outside the diameter of the hole were the primary contribution to the correction. A small additional correction was calculated to account for δ rays from the secondary pion or electron in the air near the counter which could strike the inside edge of the hole in the scintillator. The δ -ray correction was estimated by a Monte Carlo calculation and included the experimental geometry, the effects of multiple Coulomb scattering, and the efficiency of A_5 for detecting a low-energy δ ray incident on the brass-aluminum absorber. The estimation of the correction for hard photons in A_5 also included the experimental geometry and the A_5 detection efficiency for photons. The detection efficiency of A_5 for low-energy electrons and photons with its absorber is shown in Fig. 16. These efficiencies were estimated from measurements of the counter's efficiency made with electrons between 20 MeV, and 100 MeV, and from calculations with a microscopic-shower-development program called EGS.¹³ The contribution of hard photons in A_5 to the radiative correction was estimated to be 0.35%. The correction for δ rays striking A_5 was $(0.39 \pm 0.04)\%$. The error is dominated by the detection efficiency of A_5 .

Beam-associated accidental anticoincidences in A_5 were eliminated electronically. This was possible by virtue of the rf structure in the beam spill and the very stringent requirements on countable beam discussed earlier. The only accidental vetoes possible from A_5 were due to random phototube noise. This rate was measured and the accidentals found to be negligible.

TABLE IV. Events, measured cross section, and form factor versus q^2 .

q^2 (GeV/c)	No. of events	Events after corrections	$(d\sigma/dq^2)_{\text{exp}}$ [$\mu\text{b}/(\text{GeV}/c)^2$]	$ F_\pi ^2 \pm \text{total error}$
0.0317	1420	2016	148.3	0.903 \pm 0.026
0.0337	1247	1726	126.9	0.910 \pm 0.027
0.0358	1083	1503	110.5	0.927 \pm 0.030
0.0378	992	1374	101.0	0.988 \pm 0.033
0.0399	782	1093	80.3	0.911 \pm 0.034
0.0419	683	964	70.9	0.930 \pm 0.038
0.0439	550	790	58.1	0.879 \pm 0.039
0.0460	483	688	50.6	0.881 \pm 0.040
0.0480	420	598	43.9	0.880 \pm 0.043
0.0501	383	547	40.3	0.927 \pm 0.047
0.0521	348	501	36.8	0.971 \pm 0.052
0.0542	284	410	30.1	0.915 \pm 0.054
0.0562	196	287	21.1	0.735 \pm 0.053
0.0583	176	263	19.4	0.779 \pm 0.059
0.0603	172	250	18.4	0.853 \pm 0.065
0.0623	150	219	16.1	0.870 \pm 0.071
0.0644	120	177	13.0	0.818 \pm 0.075
0.0664	101	150	10.9	0.813 \pm 0.081
0.0685	83	122	9.0	0.790 \pm 0.087
0.0705	66	100	7.3	0.768 \pm 0.095

There is a possible correction for backscattering from the target into the beam halo counter A_H . This was eliminated during data taking by keeping the beam telescope coincidence width short. Particles which back scattered from the target arrived too late to veto the event. The various beam kills coupled with the 18.6-nsec rf structure prevented accidental backscattering vetoes.

IV. FORM-FACTOR RESULTS

The square of the form factor of the pion $|F_\pi(q^2)|^2$ is defined as the ratio $|F_\pi(q^2)|^2 = (d\sigma/dq^2)_{\text{exp}}/(d\sigma/dq^2)_{\text{pt}}$ where $(d\sigma/dq^2)_{\text{exp}}$ is the experimental differential cross section including all corrections, and $(d\sigma/dq^2)_{\text{pt}}$ is the theoretically

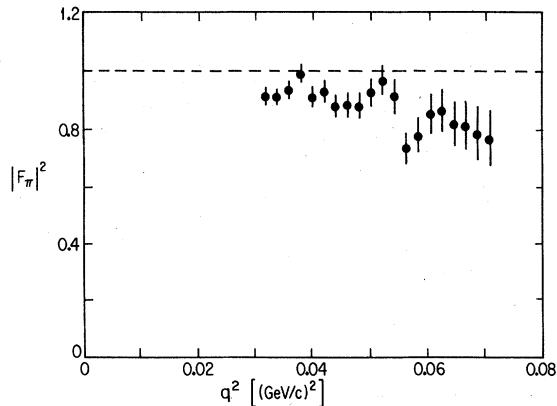


FIG. 17. The square of the pion form factor versus q^2 .

expected differential cross section for a negatively charged pion with no spatial extent.

Our experimental results for $|F_\pi(q^2)|^2$ are given in Table IV, and plotted in Fig. 17. The errors in the table and figure were obtained by adding the statistical and systematic error in quadrature.

In order to treat the experimental errors optimally, we have calculated the symmetric error matrix M_{ij} whose correlation coefficients are $\rho_{ij} = M_{ij}/(M_{ii}M_{jj})^{1/2}$. The diagonal elements of the error matrix M_{ij} are just the squares of the total errors listed in Table IV. The values for the elements ρ_{ij} are given in Table V. The error matrix M_{ij} includes the correlated error among the data as well as the overall systematic error. Systematic errors were treated as introducing a maximal positive correlation between all pairs

TABLE V. ρ_{ij} correlation coefficients times 1000. The matrix is symmetric with $\rho_{i=j}=1$. Examples: $\rho_{18} = 0.079$; by interpolation $\rho_{28} = 0.075$.

$i \backslash j$	1	3	5	7	9	11	13	15	17	19
2	126	111	94	79	69	62	47	43	36	30
4	112	99	85	71	62	56	42	39	33	27
6	94	83	71	60	52	48	36	33	28	23
8	79	70	60	51	44	40	31	29	24	20
10	70	62	53	45	40	36	27	26	22	18
12	59	53	46	39	34	31	24	22	19	16
14	46	41	36	31	27	25	19	18	15	13
16	42	38	33	28	25	23	18	17	14	12
18	34	31	27	23	21	19	14	14	12	10
20	28	25	22	19	17	15	12	11	9	8

TABLE VI. The values obtained for $\langle r_\pi^2 \rangle$ which minimize χ^2 using the M_{ij} error matrix fit.

	$ F_\pi(q^2) ^2$	$\langle r_\pi^2 \rangle$
Pole form	$(1 + \frac{1}{6}\langle r_\pi^2 \rangle q^2)^{-2}$	$0.31 \pm 0.04 \text{ fm}^2$
Dipole form	$(1 + \frac{1}{12}\langle r_\pi^2 \rangle q^2)^{-4}$	$0.31 \pm 0.04 \text{ fm}^2$
Linear form	$(1 - \frac{1}{6}\langle r_\pi^2 \rangle q^2)^2$	$0.30 \pm 0.04 \text{ fm}^2$

of data points with the exception of the geometrical efficiency. The geometrical efficiency was assumed to correlate only nearby data points near the low- q^2 and high- q^2 ends of the data spectrum where the efficiency deviated significantly from unity (see Fig. 15).

A χ^2 is calculated from $\chi^2 = \sum_{ij} (T_i - E_j) M^{-1}_{ij} \times (T_j - E_j)$, where the E_j 's are the experimental results for $|F_\pi(q^2)|^2$ and the T_i 's are the theoretical form for $|F_\pi(q^2)|^2$.

Several theoretical forms were assumed for T_i . These forms along with the results of the fits are listed in Table VI. In these fits the normalization error has been included in the matrix M_{ij} . A minimum in χ^2 was obtained by varying the parameter $\langle r_\pi^2 \rangle$ in the fit. The $\langle r_\pi^2 \rangle$ value at the minimum is quoted as our best fit value; its error was obtained by locating the values of $\langle r_\pi^2 \rangle$ which increase χ^2 by one unit from its minimum value. This method efficiently treats the statistical errors, the overall systematic errors, and the correlations between neighboring data points. The result is seen to be insensitive to the assumed shape of $|F_\pi(q^2)|^2$. Our final result is

$$\langle r_\pi^2 \rangle = 0.31 \pm 0.04 \text{ fm}^2 \quad (4.1)$$

or

$$\langle r_\pi^2 \rangle^{1/2} = 0.56 \pm 0.04 \text{ fm}. \quad (4.2)$$

The sensitivity of $\langle r_\pi^2 \rangle$ to the overall normalization of the $|F_\pi(q^2)|^2$ data was investigated. It was found that a change of $\pm 1\%$ in the normalization of the $|F_\pi(q^2)|^2$ data results in a change in $\langle r_\pi^2 \rangle$ of $\pm 0.028 \text{ fm}^2$.

V. CONCLUSION

Our results for $|F_\pi(q^2)|^2$ represent a considerable improvement over all previous attempts to measure the electromagnetic radius of the pion by direct πe scattering.² In addition our result for $\langle r_\pi^2 \rangle$ is determined by purely experimental means and does not depend on any specific theoretical model for its interpretation.

The result of this experiment disagrees with the results from single-pion electroproduction. The most recent electroproduction result¹⁴ is $\langle r_\pi^2 \rangle = 0.51 \pm 0.03 \text{ fm}^2$ and differs from our result, $\langle r_\pi^2 \rangle = 0.31 \pm 0.04 \text{ fm}^2$. A possible explanation for this discrepancy, apart from the fact that extracting the pion form factor from single-pion electroproduction data is model dependent, is that the electroproduction data is in the q^2 range $0.18 \leq q^2 \leq 3.99 \text{ (GeV/c)}^2$ and does not as directly measure the slope of $|F_\pi(q^2)|^2$ at $q^2 = 0$. Our experiment is in the q^2 range $0.03 \leq q^2 \leq 0.07 \text{ (GeV/c)}^2$ and is a more direct measurement of the slope of $|F_\pi(q^2)|^2$ at $q^2 = 0$ and, hence, $\langle r_\pi^2 \rangle$.

Our result is consistent with the requirements of analyticity which connect the timelike and spacelike behavior of the pion form factor.^{2,15} It is also consistent with the vector-dominance model. A calculation of Cho and Sakurai¹⁶ yields $0.34 \leq \langle r_\pi^2 \rangle \leq 0.48 \text{ fm}^2$. Our result may also be compared with the Chou-Yang model. A calculation based on elastic-scattering data up to 200 GeV (Ref. 17) yields $\langle r_\pi^2 \rangle^{1/2} = 0.61 \pm 0.03 \text{ fm}$ which agrees well with the result of our measurement $\langle r_\pi^2 \rangle^{1/2} = 0.56 \pm 0.04 \text{ fm}$.

ACKNOWLEDGMENTS

We are grateful for the assistance and encouragement of the directorate and staff of Fermilab. The Dubna participants are grateful for the assistance of the directorate of the Joint Institute for Nuclear Research. We thank Dr. Charles Buchanan, Jonathan Kubic, and Jim Volk for their aid.

The experiment was supported in part by the U.S. Department of Energy and by the U.S. National Science Foundation.

*Now at Varian Associates, Hansen Way, Palo Alto, CA 94306.

†Deceased.

‡Now at Physics Department, Johns Hopkins University, Baltimore, MD 21218.

§Now at Interand Corp., 450 E. Ohio, Chicago, IL 60611.

||Now at the Physics Department, University of California at Riverside, CA 92502.

¶Now at North Central College, Naperville, IL 60540.

**Now at High Energy Physics Laboratory, Stanford University, Stanford, CA 94305.

††Now at the Institute of Atomic Physics, Bucharest, Romania.

¹E. B. Dally *et al.*, Phys. Rev. Lett. **39**, 1176 (1977).

²G. T. Adylov *et al.*, Phys. Lett. **51B**, 402 (1974); G. T. Adylov *et al.*, Nucl. Phys. **B128**, 461 (1977).

³C. F. May, Ph. D. Dissertation, UCLA, 1977 (unpublished).

- ⁴C. A. Rey, R. J. Wojslaw, J. A. Poirier, and J. T. Volk, Nucl. Instrum. 157, 401 (1978).
- ⁵J. A. Poirier, C. A. Rey, J. T. Volk, and R. J. Wojslaw, Nucl. Instrum. 153, 105 (1978).
- ⁶R. Yamada *et al.*, Nucl. Instrum. 138, 567 (1976).
- ⁷This unit was designed and built by G. Kerns of Fermilab.
- ⁸W. T. Eadie *et al.*, *Statistical Methods in Experimental Physics* (North-Holland, Amsterdam, 1972); O. Dahl *et al.*, LBL Alvarez Group Programming Note P-126 (unpublished).
- ⁹G. T. Adylov *et al.*, Nucl. Phys. B128, 461 (1977); D. Yu. Bardin and N. M. Shumeiko, JINR Report No. P2-8975, 1975 (unpublished); D. Yu. Bardin, V. B. Semikov, and N. M. Shumeiko, Yad. Fiz. 10, 1020 (1969) [Sov. J. Nucl. Phys. 10, 586 (1970)].
- ¹⁰Y. Tsai, Rev. Mod. Phys. 46, 815 (1974).
- ¹¹D. Yu. Bardin *et al.*, JINR Report No. E2-6235, 1972 (unpublished).
- ¹²S. P. Denisov *et al.*, Nucl. Phys. B61, 63 (1973); A. S. Carroll *et al.*, Phys. Rev. Lett. 33, 932 (1974); Fermilab Single Arm Spectrometer Group, Phys. Rev. Lett. 35, 1195 (1975).
- ¹³R. L. Ford and W. R. Nelson, Report No. SLAC-PUB-210, 1978 (unpublished).
- ¹⁴C. J. Bebek *et al.*, Phys. Rev. D 17, 1693 (1978).
- ¹⁵D. Levin and S. Okubo, Phys. Rev. D 6, 3149 (1972).
- ¹⁶C. F. Cho and J. J. Sakurai, Lett. Nuovo Cimento 2, 7 (1971).
- ¹⁷T. T. Chou, Phys. Rev. D 19, 3327 (1979).